Direct Visualization of Fast Surface Ion

Diffusion in Vanadium Dioxide Nanowires

Yasen Hou, <sup>1</sup> Rui Xiao, <sup>1</sup> Xin Tong, <sup>2</sup> Scott Dhuey, <sup>3</sup> and Dong Yu<sup>1\*</sup>

<sup>1</sup>Department of Physics, University of California, Davis, California 95616, United States

<sup>2</sup>School of Physics, Peking University, Beijing 100871, People's Republic of China

<sup>3</sup>The Molecular Foundry, Lawrence Berkeley National Laboratory, Berkeley, California 94720,

**United States** 

\*E-mail: yu@physics.ucdavis.edu

Keywords: vanadium dioxide, metal insulator transition, ionic liquid gating, ion diffusion,

scanning photocurrent microscopy, nanowires

**Abstract:** We investigate *in-situ* ion diffusion in vanadium dioxide (VO<sub>2</sub>) nanowires (NWs) by

using photocurrent imaging. Alkali metal ions are injected into a NW segment via ionic liquid

gating and are shown to diffuse along the NW axis. The visualization of ion diffusion is realized

by spatially resolved photocurrent measurements, which detect the charge carrier density change

associated with the ion incorporation. Diffusion constants are determined to be on the order of

1

10<sup>-10</sup> cm<sup>2</sup>/s for both Li<sup>+</sup> and Na<sup>+</sup> ions at room temperature, while H<sup>+</sup> diffuses much slower. The ion diffusion is also found to occur mainly at the surface of the NWs, as metal contacts can effectively block the ion diffusion. This novel method of visualizing ion distribution is expected to be applied to study ion diffusion in a broad range of materials, providing key insights on phase transition electronics and energy storage applications.

Vanadium dioxide (VO<sub>2</sub>), an exemplary correlated material, undergoes a metal-insulator phase transition (MIT) accompanied by a structural transition from high-temperature rutile to low-temperature monoclinic lattice when cooled below 340 K.<sup>1-4</sup> The MIT exhibits a rapid and drastic change in the electronic and optical properties, based on which novel applications of switching,<sup>5-8</sup> sensing,<sup>9, 10</sup> and resonators<sup>11, 12</sup> have been intensively pursued. Ultrafast<sup>13-15</sup> and microscopic<sup>2, 16, 17</sup> techniques, along with improved computational approaches, <sup>18</sup> have been employed to clarify on the phase transition mechanisms. Ionic liquid (IL) gating 19-28 and chemical doping<sup>29-33</sup> of VO<sub>2</sub> are of particular interest as they can effectively modulate MIT for potential Mott transistors<sup>2, 34</sup> and create unusual electronic phases.<sup>22</sup> Though the underlying mechanism for IL gating is still under debate, diffusion of atoms, either hydrogen diffusion that leads to chemical doping 19-21 or oxygen diffusion that creates oxygen vacancies, 22-25 is generally considered to play a significant role. For example, IL gating induced MIT in VO2 has been attributed to electrochemical reaction involving oxygen vacancies. 22 which have been found to diffuse at least 0.5  $\mu$ m along the rutile c axis. <sup>25</sup> H atoms also result in the stabilization of the metal phase down to 2 K, and the diffusion constant of H has been determined to be around 10<sup>-10</sup> cm<sup>2</sup>/s at 100 ° C along the rutile c axis and is much slower along the a axis.  $^{29,35}$ 

Though diffusion of atoms in VO<sub>2</sub> is at the heart of the modulation of the MIT through IL gating or doping, their studies have been limited to hydrogen and oxygen to date. Alkali metals such as Li, Na, and K are also widely used in IL gating. <sup>27, 28, 36-39</sup> Exploration of their diffusion in room temperature monoclinic VO2 not only sheds light on the IL gating mechanism, but also provides realistic approaches to manipulate the MIT towards applications. Furthermore, diffusion may occur both in bulk and at surface. As the micro- and nano-electronic devices approach to ever smaller scale, surface becomes more important. While our understanding of bulk diffusion in solid has advanced greatly, diffusion at surface is notoriously challenging to investigate, 40 though it is critical to an endless list of phenomena at nanoscale such as catalysis, 41 crystal growth, 42, 43 and many self-assembly and filtration processes. 44, 45 Surface diffusion is also particularly important to the application of Li and Na batteries, 46 since the electrodes are often made of polycrystalline materials where the ion diffusion is often dominated at the domain boundaries. Sophisticated experimental techniques such as scanning tunneling microscopy (STM), <sup>47, 48</sup> field ion microscopy (FIM), <sup>49, 50</sup> and helium atom scattering <sup>51</sup> have been developed to probe the atomic scale absorbate diffusion. However, these techniques generally require ultrahigh vacuum and ultraclean atomically flat surface, and thus are challenging to apply to study ion diffusion in realistic environment such as in ambient condition and in electrolyte solution.

In this *letter*, we report the direct visualization of ion diffusion in single crystalline VO<sub>2</sub> nanowires (NWs) by taking advantage of the drastic change in charge carrier concentration associated with ion doping. The ions are injected from electrolyte into an exposed segment of a VO<sub>2</sub> NW by electrochemical gating, while the direct ion doping of the other part of the NW is prohibited by an ion barrier. The diffusion of the ions from the exposed segment to the covered

segment along the NW axis significantly increases the local electron concentration. The imaging of such change is then made possible by using scanning photocurrent microscopy (SPCM), where photocurrent generated by local illumination is mapped as a function of laser position. Using this novel method, we image the ion transport in VO<sub>2</sub> NWs *in-situ* and extract diffusion constants for Li, Na, and H ions at room temperature.

Single crystalline VO<sub>2</sub> NWs are synthesized by a chemical vapor deposition (CVD) method following our previous work as briefed in the Method session.<sup>28</sup> Figure S1 shows the morphology of the as-grown VO<sub>2</sub> NWs. The NWs have rectangular cross-sections and are typically 300-500 nm in width and 100-300 nm in height, and tens of µm's long. They grow along the [100] direction of the monoclinic (M1) phase, which corresponds to the c axis of the high temperature rutile phase.<sup>28</sup> The as-grown NWs are then transferred to 300 nm SiO<sub>2</sub> covered Si substrates, where single NW field effect transistor (FET) devices are fabricated using a standard electron beam lithography (EBL) process. To enable local injection of ions into the NW, a poly (methyl methacrylate) (PMMA) layer is spin-coated on top of the FET device and is partially removed by EBL to expose only a segment of the NW. Finally, an IL droplet of polyethylene glycol (PEO) with 5 wt % of LiClO<sub>4</sub> is applied to the NW device (the detailed information of chemicals can be found in Method). Figure 1a shows the schematic drawing of a complete device. Optical images of a typical device before and after the application of IL are shown in Figures 1b and 1c. A window is clearly seen in Figure 1b where the PMMA is locally removed and the NW is exposed. This window cannot be seen in Figure 1c after a droplet of LiClO<sub>4</sub>/PEO is placed on the device because the refractive index of PEO matches well with that of PMMA. The IL is only in direct contact with the exposed NW segment while the other part of the NW is protected by the PMMA layer.

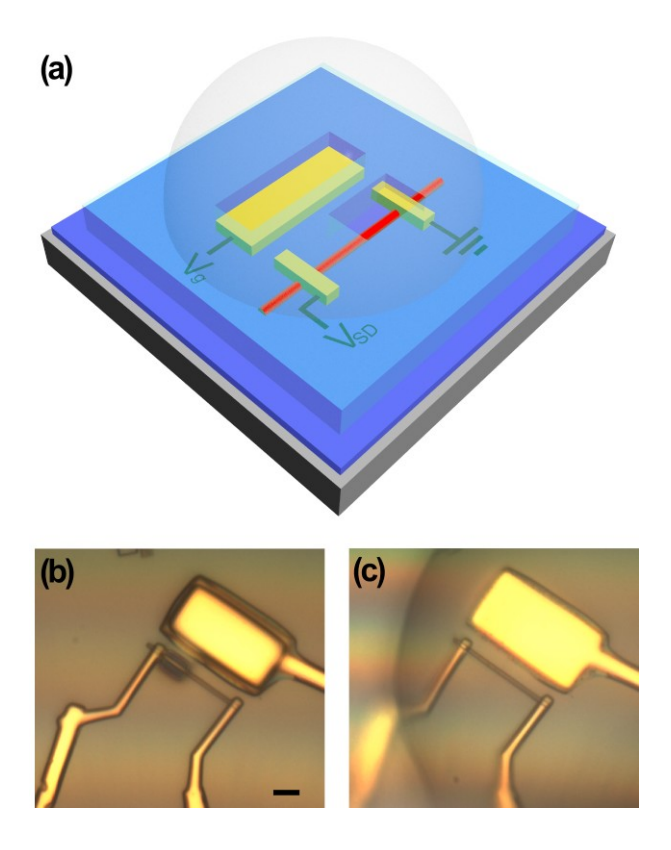


**Figure 1**. VO<sub>2</sub> NW device configuration with an ion-injection window. (a) Schematic drawing of the device, where a VO<sub>2</sub> NW (red line) is electrically connected to Cr/Au contacts (golden bars) and partially covered by PMMA (light blue layer). An IL droplet (half dome) is then applied to cover the entire device but is only in direct contact to a segment of the VO<sub>2</sub> NW through a window. (b) and (c) are optical images of a typical device before and after applying IL. The scale bar denotes 5 μm.

We first compare the IL gating effects in a fully exposed channel and a partially exposed channel in a VO<sub>2</sub> NW device (Device #L1, reflection image shown Figure 2b). Electrochemical gate sweeps of this three-probe device are shown in Figure 2a. As the gate voltage ( $V_g$ ) is increased to 1 V, the conductance of the fully exposed section (G23) is enhanced by over 30 times, indicating insulator-to-metal phase transition. On the contrary, the conductance of the partially exposed section (G12) is only doubled, indicating that the resistance of the NW segment covered by PMMA is unaffected by gating.

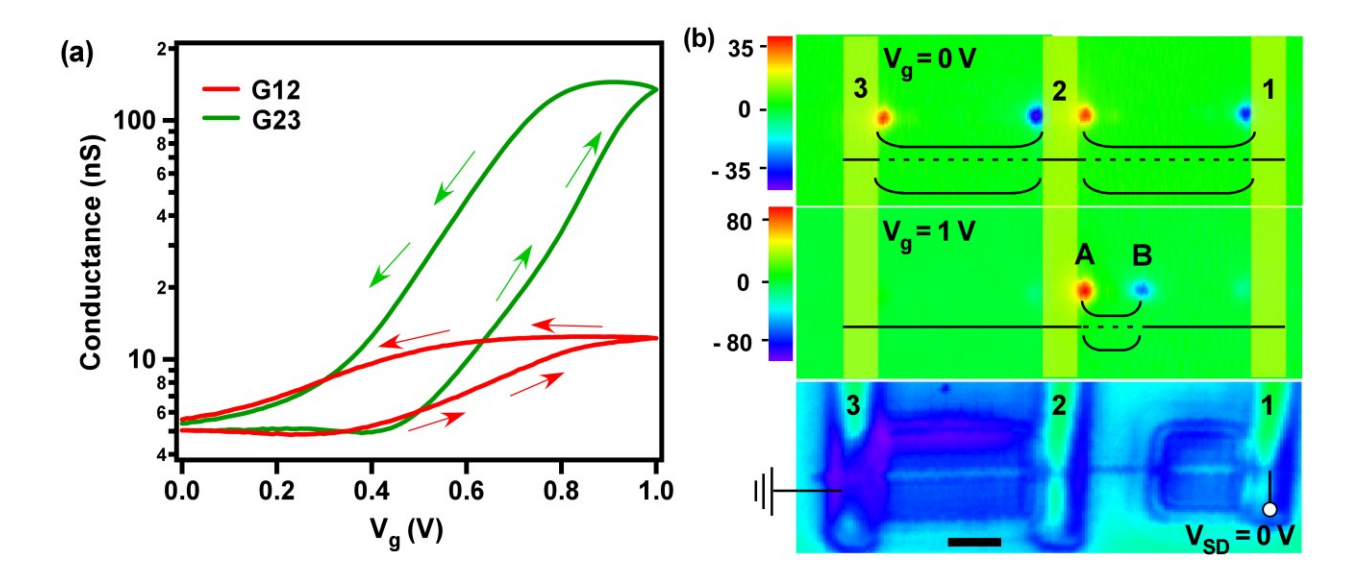


**Figure 2.** Electrochemical gating and SPCM characterizations of a single VO<sub>2</sub> NW FET device (Device #L1) partially covered by PMMA. (a) The conductance between contacts 1 and 2 (G12) and the conductance between contacts 2 and 3 (G23) as a function of  $V_g$ . The arrows indicate the scan direction. Scan rates for both curves are 20 mV/s. (b) Photocurrent images of the device at different  $V_g$ . The scale bar at the bottom is 2 μm and the color scales are in pA. The laser at 532 nm has a peak intensity of 30 kW/cm<sup>2</sup>. The yellow shaded areas indicate the positions of the electrodes. The band bending diagrams are overlay with the photocurrent images. The bottom panel shows the reflection image before applying IL.

SPCM measurements are then performed to extract the gate-induced doping distribution. SPCM provides spatially resolved photocurrent mapping and has been used to explore charge carrier transport in various nanostructures.  $^{52\text{-}61}$  The experimental setup is briefly described in the Method and detailed in our previous work.  $^{60}$  All measurements are performed in air and at room temperature. Though pure PEO solidifies at room temperature, it stays in the liquid phase after adding salt such as LiClO<sub>4</sub> and remains transparent, allowing photocurrent imaging. In the SPCM measurements, electrodes 1 and 3 are short-circuited while electrode 2 is floating. At  $V_g = 0$  V, photocurrent spots of opposite polarities are observed near metal-NW contacts (Figure 2b), attributed to photovoltaic effects at Schottky junctions.  $^{28}$ ,  $^{62}$  Polarities of the spots indicate upward band bending toward the metal electrodes. Then a SPCM image is taken immediately

after  $V_g$  is increased to 1 V, in which the photocurrent spots at the contacts exposed to IL disappear, while the photocurrent spot at the contact covered by PMMA (spot A in Figure 2b) remains. This is because gating only induces insulator-to-metal phase transition in the exposed NW segment and eliminates the Schottky junction at the corresponding contacts. The photocurrent magnitude at spot A is also increased from 35 to 80 pA, because the total channel resistance is reduced. In addition, another photocurrent spot appears at the window edge (spot B) and its polarity indicates the band bends upwards towards the gate induced VO<sub>2</sub> metal state. All these observations indicate that PMMA effectively blocks the ions from entering the covered NW, which is expected as baked PMMA forms a chemically inert and mechanically robust layer. This PMMA layer proves to be quite stable in a control test: the conductance of a VO<sub>2</sub> NW device fully covered by PMMA remains the same even after a high gate voltage ( $V_g = 62.5 \text{ V}$ ) is applied for 7 hours (Figure S2). A similar blocking effect of photoresist has also been shown in a recent study of ion transport in H<sub>2</sub>V<sub>3</sub>O<sub>8</sub> NWs.<sup>63</sup>

After demonstrating the ion blocking capability of PMMA, we now present the results for ion diffusion in another VO<sub>2</sub> NW device (Device #L2). As  $V_g$  is increased to 1 V in this device, a photocurrent spot is immediately observed at the window edge (Figure 3a), consistent with the results in Device #L1. Strikingly, when fixing  $V_g$  at 1 V for a few minutes, we notice the appearance of an additional photocurrent spot of opposite polarity, which gradually broadens and shifts from the window edge into the PMMA covered NW segment. In 40 minutes, the spot moves across the entire NW channel ( $\sim$  8 µm long). As a side note, photocurrent is also observed along the edge of the right electrode under  $V_g = 1$  V, presumably caused by the light induced electrochemical reaction on metal. The long-time gating does not affect the morphology of the VO<sub>2</sub> NW. The atomic force microscopic (AFM) images of the device before and after applying

 $V_{\rm g}=1~{
m V}$  for 1 hour look identical (Figure S3). Careful examination reveals that there is a slight height reduction about 2 - 4 nm in the exposed 270 nm-thick NW segment, likely caused by electrochemical etching of the surface. But the PMMA covered NW segment has no change in height at all.

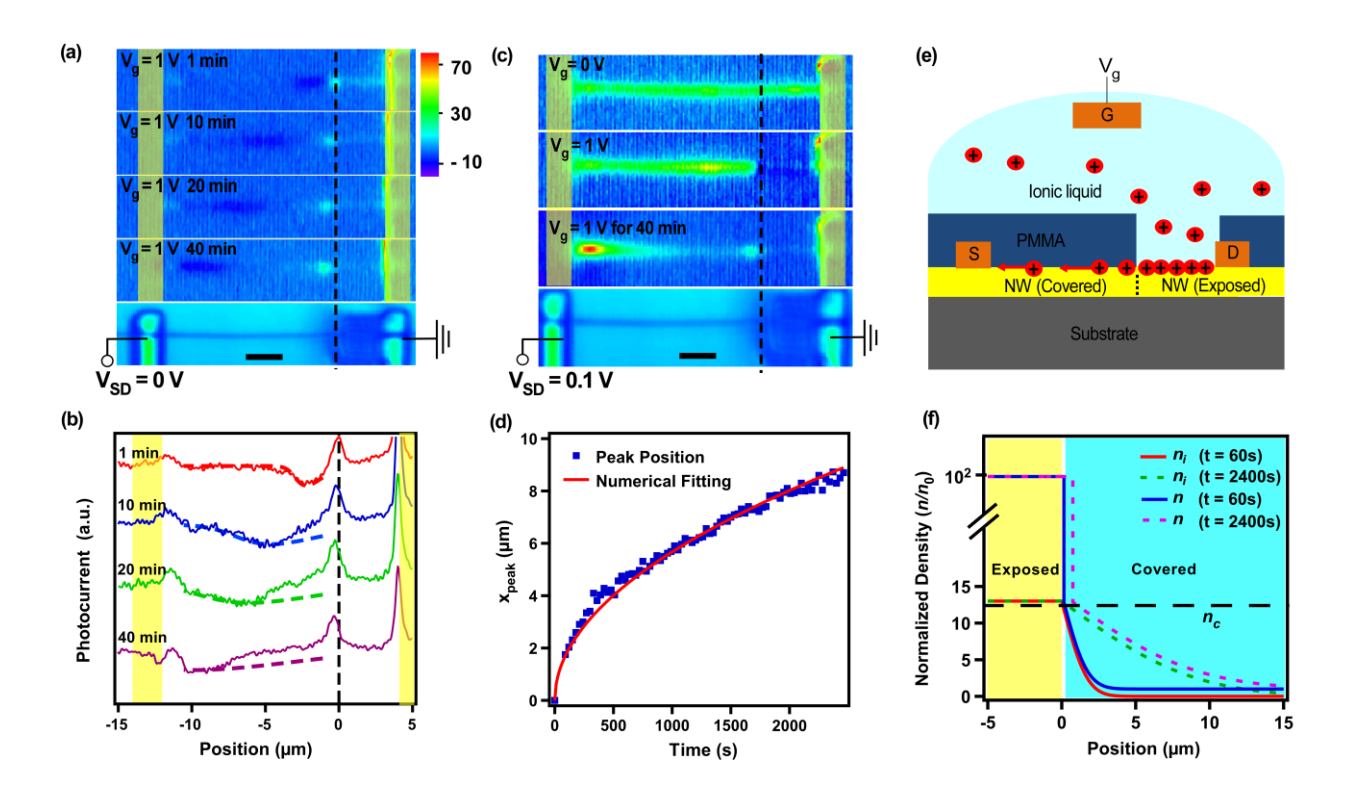


Figure 3. SPCM visualization of the Li<sup>+</sup> ion transport in a VO<sub>2</sub> NW device (Device #L2). (a) Photocurrent images at  $V_g = 1$  V and  $V_{SD} = 0$  V as a function of gating time. The scale bar denotes 2 μm and the color scale is in pA. (b) Photocurrent cross sections (solid lines) along the NW axis extracted from (a) and the calculated electric field distributions (dashed lines) at different time. The yellow shaded areas indicate the positions of the electrodes and the dashed line indicates the window edge. (c) Photocurrent images at  $V_{SD} = 0.1$  V taken at  $V_g = 0$  V, immediately, and 40 min after  $V_g$  is increased to 1 V, respectively. (d) The peak position of the shifting photocurrent spot as a function of gating time. The red solid line is the calculated peak position values using parameters  $D = 1.0 \times 10^{-10}$  cm<sup>2</sup>/s and  $n_{i0}/n_0 = 13$ . This calculated curve overlaps perfectly with a simple square root fitting ( $x_{\text{peak}} = \sqrt{D^*t}$ ), where  $D^* = 3.1 \times 10^{-10}$  cm<sup>2</sup>/s. (e) Schematic illustrating ion injection into the exposed NW and subsequent diffusion into the covered NW. S and D are source and drain metal contacts, respectively. (f) Electron density (n) and ion density (n) as a function of position away from the window, at two different gating times.

We will first provide a qualitative physical picture to explain the observed shifting photocurrent spot. The occurrence of this photocurrent spot in the PMMA covered VO<sub>2</sub> NW segment indicates that an internal electric field is developed by gate induced ion injection. As the direct vertical Li<sup>+</sup> ion injection is blocked by the PMMA layer, ions must diffuse from the exposed segment along the NW axis. The ion concentration is high in the exposed NW segment and gradually drops over distance moving into the covered region. As the positive ions induce free electrons in the NW, this ion concentration gradient leads to an electron concentration gradient and an internal electric field. At fixed gate voltage, more ions diffuse into the covered NW segment and result in broadening and shift of the photocurrent spot. At 40 min, the negative photocurrent spot shifts all the way to the left electrode, suggesting ions diffuse through the entire NW channel. Therefore, these sequential photocurrent images allow one to observe the *insitu* ion diffusion in motion. The photocurrent peak position ( $x_{peak}$ ) as a function of gating time can be fit nicely by a square root function ( $x_{peak} = \sqrt{D^*t}$ ), where  $D^* = 3.1 \times 10^{-10}$  cm<sup>2</sup>/s is the apparent diffusion constant (Figure 3d).

The SPCM images under non-zero  $V_{\rm SD}$  (Figure 3c) further confirm this physical picture. Since photocurrent distribution reflects the local electric field distribution, at non-zero  $V_{\rm SD}$ , the most resistive part of the NW has the largest potential drop and hence the strongest photocurrent. Before  $V_{\rm g}$  is applied, the photocurrent is uniform under  $V_{\rm SD}=0.1$  V, indicating a uniform distribution of electric field. Immediately after  $V_{\rm g}=1$  V is applied, the photocurrent in the exposed segment disappears, since this segment is switched to metal phase and its resistance is greatly reduced. After fixing  $V_{\rm g}=1$  V for 40 min, photocurrent is also greatly suppressed in the covered NW segment close to the window, indicating Li<sup>+</sup> diffuses into this region and leads to a resistance reduction.

To quantitatively understand the measured photocurrent profiles and to more accurately extract the ion diffusion constant, we provide a simple model based on 1D ion diffusion along the NW axis. The ion concentration ( $n_i$ ) along the NW axis is expected to be governed by Fick's second law,

$$\frac{\partial n_i}{\partial t} = D \frac{\partial^2 n_i}{\partial x^2} \tag{1}$$

where D is the diffusion constant, t is time, and x is the distance. The solution is,

$$n_i(x,t) = n_{i0} \operatorname{erfc}(\frac{x}{2\sqrt{Dt}})$$
 (2)

where  $n_{i0}$  is the ion concentration at the boundary (x = 0) and erfc is the complementary error function. Assuming each positive ion induces a free electron and  $n_0$  is the electron concentration before  $V_g$  is applied, the total free electron concentration is then  $n = n_0 + n_i$ . The erfc distributions of n and  $n_i$  are plotted in Figure 3f. At t = 60 s after gating, the exposed NW segment is switched to metal phase when  $n > n_c$  ( $n_c$  is the critical electron concentration to induce insulator-to-metal transition), leading to a drastic increase of n to about  $10^2 n_0$ . A junction is then created between the metal and insulator domains, which explains the positive photocurrent spot observed at the window edge. The distribution of n caused by the ion diffusion explains the negative photocurrent spot inside the covered segment. At t = 2400 s, ions further diffuse into the covered NW segment. This leads to a slight expansion of the metal domain into the covered segment, evidenced by the slight shift of the positive photocurrent spot at the window edge (Figure 3a). It also results in a shift and broadening of the negative photocurrent spot as the distribution of n extends further into the covered segment.

If n is low compared with the density of states ( $N_c$ ), we can use Boltzmann distribution to calculate the local electric potential  $\varphi$  by,

$$n(x,t) = N_C \exp\left[-\frac{E_C - E_F - |e|\varphi}{k_B T}\right]$$
(3)

where  $E_c$  is the energy level of the conduction band edge,  $E_F$  is the Fermi level, |e| is the absolute value of electron charge,  $k_B$  is the Boltzmann constant, and T is the temperature. Therefore, the local electric field caused by the gate-injected ions is,

$$E(x,t) = -\frac{d}{dx}\varphi = -\frac{k_B T}{|e|}\frac{d}{dx}\ln n = -\frac{k_B T}{|e|}\frac{d}{dx}\ln \left[n_0 + n_{i0}\operatorname{erfc}\left(\frac{x}{2\sqrt{Dt}}\right)\right]$$
(4)

As photocurrent is proportional to the local electric field, we can make a direct comparison of the measured photocurrent distribution and the electric field distribution calculated from the above model. As shown in Figure 3b, the calculated electric field follows the observed photocurrent curves quite well at various gating times.

After understanding the photocurrent distribution, we now use the above model to more accurately extract the diffusion constant. Figure 3d shows the time dependent photocurrent peak position, which corresponds to the position where electric field reaches maximum. We can then determine the D value through best fitting of the experimental data using numerically obtained electric field maximum position from Eq. (4). It turns out that the extraction of D depends on the value of  $\frac{n_{i0}}{n_0}$ , which can be estimated from the photocurrent images taken under bias since,

$$\Delta j = \Delta \sigma E = \frac{j\Delta \sigma}{\sigma} = \frac{j\Delta n}{n} \propto \frac{1}{n} \tag{5}$$

where  $\Delta j$  is the photocurrent density,  $\Delta \sigma$  is the laser-induced increase in conductivity, and the photogenerated carrier concentration  $\Delta n$  is expected to be independent of injection position.

Therefore, we may estimate  $\frac{n_{i0}}{n_0}$  by the ratio of photocurrent, which is about 13 using the photocurrent data at 40 min in Figure 3c (more details can be found in Figure S4 in the Supporting Information). By using  $\frac{n_{i0}}{n_0} = 13$  and  $D = 1.0 \times 10^{-10}$  cm<sup>2</sup>/s, the calculated  $x_{\text{peak}}$  matches very well the experimental curve (Figure 3d). We note that this model-determined D value is on the same order of magnitude as, but is expected to be more accurate than the simple square fit value ( $D^*$ ). Upon the four measured VO<sub>2</sub> NW devices, we obtained D values ranging from  $2.2 \times 10^{-11}$  to  $1.0 \times 10^{-10}$  cm<sup>2</sup>/s for Li<sup>+</sup> (see Table S1 in Supporting Information for a summary of D values measured in all devices).

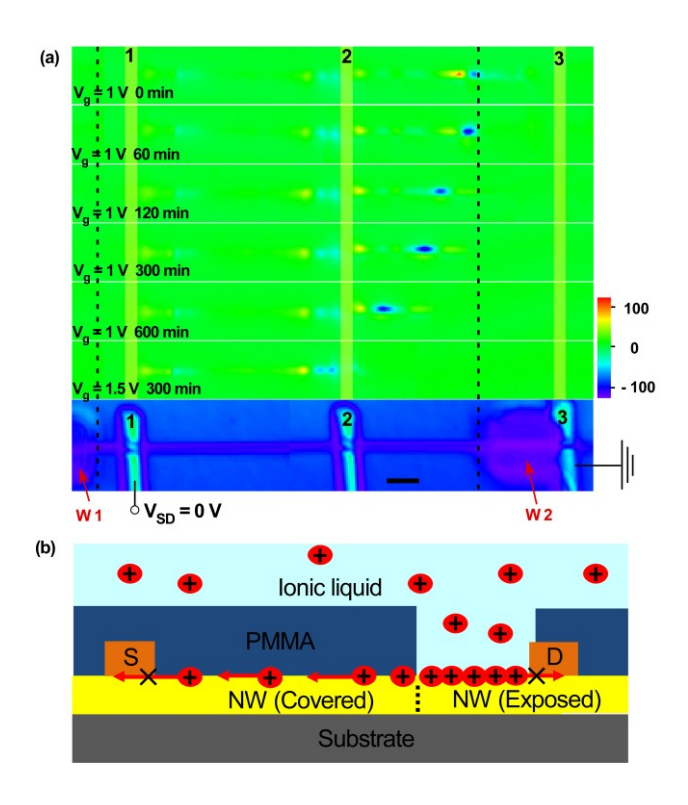


**Figure 4.** Blocking of Li<sup>+</sup> ion diffusion by metal contacts in a VO<sub>2</sub> NW device (Device #L3). (a) SPCM images as a function of time under gate voltage. The NW is covered by PMMA except two window areas W1 and W2, as shown in the reflection image at the bottom. The dashed lines indicate the window edges. The scale bar denotes 3 μm and the color scale is in pA. (b) Schematic drawing illustrates the diffusion of Li<sup>+</sup> is blocked by metal electrodes.

Next, we demonstrate that Li<sup>+</sup> ions mainly diffuse at the surface of the VO<sub>2</sub> NWs. For this purpose, we design a device (Device #L3) with two separate ion injection windows, with one window (W1) to the left of electrode 1 and the other window (W2) between electrodes 2 and 3 (Figure 4). After  $V_g = 1$  V is applied, a photocurrent spot is observed moving from the edge of W2 away from the window into the PMMA covered NW segment, similar to the behavior in Device #L2. This photocurrent spot moves across the entire channel 2-3 (11.5 μm) to electrode 2 in 600 minutes. On the other hand, an ion induced photocurrent spot is not observed in channel 1-2. Though the distance is short from the W1 edge to channel 1-2 (3.2 µm), ions injected in W1 do not appear to diffuse into the channel. This indicates that Li<sup>+</sup> diffusion is blocked by the metal electrode (Cr / Au). Even after applying a higher gate voltage ( $V_{\rm g}$  = 1.5 V) for another 300 minutes, the photocurrent distribution remains the same in channel 1-2 and the ions cannot diffuse across either electrode 1 or 2. The ion diffusion blocking by the metal contacts suggest that ions diffuse dominantly at surface. The ion diffusion in the bulk should not be stopped by the contact, as shown in the case of H<sub>2</sub>V<sub>3</sub>O<sub>8</sub>.<sup>63</sup> The surface diffusion is also supported with the fact that we do not see any optical reflection change of the NW after gating. The insulator-tometal phase transition is associated with large change in optical reflection. If ions diffuse deep into the NW, the optical reflection is expected to change significantly as observed in the case of H diffusion at elevated temperature.<sup>29</sup> However, in our case, we do not see any change in both PMMA covered segment and exposed segment even after applying  $V_{\rm g}$  for hours, indicating Li doping only occurs at the surface. Furthermore, the contact ion blocking also suggests that the ion diffusion rate at the VO<sub>2</sub> surface sensitively depends on whether the surface is covered by polymer or metal. Presumably, Cr makes stronger chemical bonding to the VO2 surface, while

the interaction between PMMA and VO<sub>2</sub> is likely much weaker, allowing Li<sup>+</sup> ions to move across.

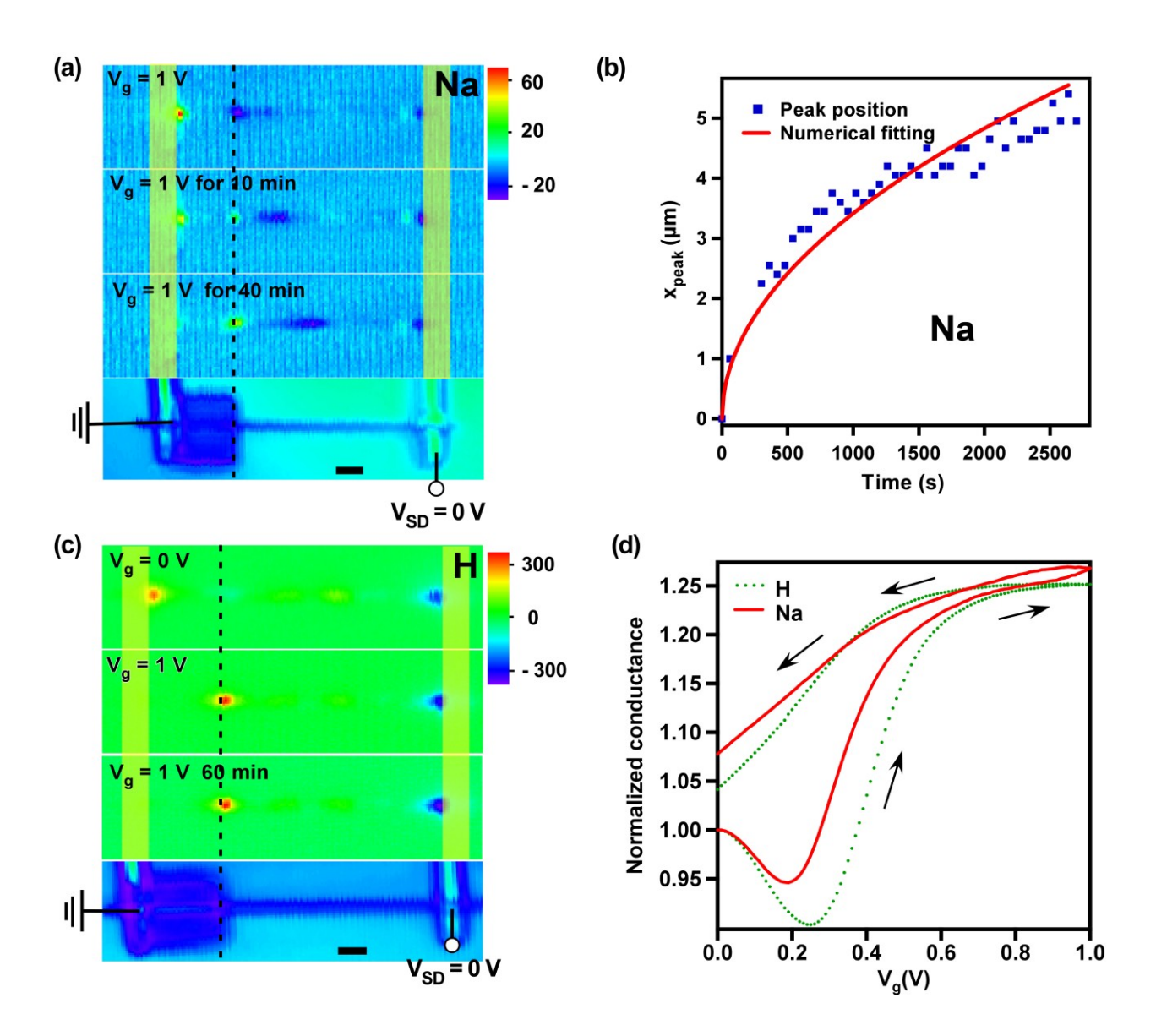


**Figure 5**. SPCM visualization of Na<sup>+</sup> and H<sup>+</sup> ion diffusion in VO<sub>2</sub> NWs. (a) Photocurrent images at  $V_g = 1$  V and  $V_{SD} = 0$  V as a function of time using NaClO<sub>4</sub>/PEO as electrolyte (Device #N1). (b) The peak position of the shifting photocurrent spot as a function of time. The red solid line is the calculated peak position values using equation (4) with  $D = 3.6 \times 10^{-11}$  cm<sup>2</sup>/s. (c) Photocurrent images at  $V_{SD} = 0$  V when using H<sub>2</sub>O/PEO as electrolyte (Device #H1). The yellow shaded areas indicate the positions of the electrodes and the dashed lines indicate the window edges. The scale bars denote 2 μm and the color scales are in pA. (d) Dark conductance as a function of  $V_g$  for devices with NaClO<sub>4</sub>/PEO and H<sub>2</sub>O/PEO, respectively. The arrows indicate the scan direction. Scan rates for both curves are 20 mV/s.

Finally, we compare the diffusion rates of different ions at the VO<sub>2</sub> surface. We first apply 5.8 wt % NaClO<sub>4</sub>/PEO to a VO<sub>2</sub> NW device with the same configuration (Device #N1), the evolution of SPCM images looks similar to LiClO<sub>4</sub>/PEO (Figure 5a). The peak positions can also be fit quite well with the simulation to extract the Na<sup>+</sup> diffusion coefficient (Figure 5b). In the three devices we measured, we obtained the D values of Na<sup>+</sup> from 3.6  $\times 10^{-11}$  to 1.6  $\times$  10<sup>-10</sup> cm<sup>2</sup>/s, comparable to Li<sup>+</sup> (see a summary of diffusion constants measured in all devices in Table S1 in Supporting Information). To test the H<sup>+</sup> ion diffusion, we apply PEO with 1 wt % H<sub>2</sub>O as the gating media to a device (Device #H1). The gating with H<sub>2</sub>O/PEO also significantly changes the conductivity of VO<sub>2</sub> (Figure 5d), akin to LiClO<sub>4</sub>/PEO and NaClO<sub>4</sub>/PEO. Similar H<sup>+</sup> ion gating effects have been shown previously. 19-21 However, different from the Li<sup>+</sup> and Na<sup>+</sup> gated devices, the photocurrent spot in this device does not appear to shift after applying  $V_g = 1 \text{ V}$  for 60 minutes (Figure 5c). If using the spatial resolution of our SPCM of 200 nm, we determine an upper limit of the D value for H<sup>+</sup> ions:  $D < 1.1 \times 10^{-13}$  cm<sup>2</sup>/s, much lower than Li<sup>+</sup> and Na<sup>+</sup>. The slower H<sup>+</sup> diffusion may be attributed to the stronger H<sup>+</sup> bonding to the VO<sub>2</sub> lattice. The sizes of Li ad Na atoms are bigger but their bonds to oxygen are weaker (bond dissociation energy,  $D_{298K}^{0}$  / (kJ mol<sup>-1</sup>) = H-O: 429.91, Li-O: 340.5, Na-O: 270).<sup>64</sup> The distinct diffusion rates of different ions also suggest our gating effect is dominated by Li<sup>+</sup> and Na<sup>+</sup> instead of oxygen vacancies from the VO<sub>2</sub>, <sup>22-25</sup> since we do not expect the diffusion constants of oxygen to depend on electrolyte. In Table 1, we compare our measured diffusion constants with the previously reported values. The D values measured in this work for Li and Na at the surface of VO2 are higher than those in bulk at room temperature as expected and are comparable to the value for surface diffusion.

**Table 1.** Ion diffusion constants in materials. (Note: \*extrapolated from high temperature measurements; \*\*estimated from data presented in the publication.)

ion	material	T (°C)	$D (\text{cm}^2/\text{s})$	surface or bulk	crystal orientation	reference
Н	ZnO	300	$8 \times 10^{-10}$	bulk	[001]	65
Н	TiO <sub>2</sub>	20	1.8×10 <sup>-13</sup>	bulk	c-axis	66*
Н	VO <sub>2</sub> NW	100	6.7×10 <sup>-10</sup>	bulk	<i>c</i> -rutile	29
О	VO <sub>2</sub> film	20	1×10 <sup>-13</sup>	bulk	<i>c</i> -rutile	25**
Li	Porous V <sub>2</sub> O <sub>5</sub>	20	3.8×10 <sup>-9</sup>	surface	N.A.	67
Li/Na	VO <sub>2</sub> NW	20	$10^{-10}$	surface	<i>c</i> -rutile	this work

In summary, we have obtained *in-situ* visualization of ion diffusion in VO<sub>2</sub> NWs, by using a novel experimental technique combining ionic liquid gating and photocurrent mapping. Photocurrent spot, representing the local electric field induced by the ion concentration gradient, gradually shifts from the ion injection source. The position shift and the broadening of the photocurrent peak quantitatively agree with a simple ion diffusion model, from which diffusion constants are extracted. We report a high diffusion constant of 10<sup>-10</sup> cm<sup>2</sup>/s for both Li<sup>+</sup> and Na<sup>+</sup> ions. The diffusion most likely occurs at the VO<sub>2</sub> surface evidenced by the effective ion diffusion blocking at the Cr/VO<sub>2</sub> interface. The ion diffusion rate of H is much slower. The observed fast ion surface diffusion in VO<sub>2</sub> provides critical insights in understanding the gate induced phase transition and may also have impacts in energy storage applications. The developed experimental method may be applied to study ion diffusion in a broad range of materials.

## Methods

 $VO_2$  NWs were synthesized via a chemical vapor deposition (CVD) method using  $V_2O_5$  as the precursor in a tube furnace (Lindberg Blue M).  $V_2O_5$  (Alfa Aesar, 99.99%) powder was adopted as the only precursor and placed in a quartz boat at the center of the tube furnace. An unpolished x-cut quartz substrates (MTI) was placed 7 cm downstream from the boat. The

system was first pumped down to a base pressure of ~30 mTorr. The furnace was then heated up to 880 ° C and maintained at the peak temperature for 40 minutes to 2 hours. After that, the furnace was cooled down to room temperature over approximately 3 hours.

In order to fabricate single NW field effect transistors (FETs), the free-standing NWs were transferred onto 300 nm SiO<sub>2</sub> coated, heavily p-doped Si wafers by directly pressing the Si wafer against the growth substrate. Subsequently, top metal contacts (250 nm Cr / 50 nm Au) were made to individual NWs using electron beam lithography (EBL, FEI 430 NanoSem) or sputtering (Lesker). A 1.5 μm thick poly (methyl methacrylate) (PMMA 950, C9, MicroChem) layer was then spin-coated at 4000 RPM on top of the device, followed by baking at 180 °C for 5 minutes. Then a second EBL was performed, followed by developing to partially remove PMMA, to expose the gate electrode and only a part of the NW. Finally, an ionic liquid droplet of polyethylene glycol (PEO, 1,000, Alfa Aesar) with 5 wt % of LiClO<sub>4</sub> (Alfa Aesar, 99%), 5.8 wt % of NaClO<sub>4</sub> (Alfa Aesar, 98%), or 1.0 wt % H<sub>2</sub>O, was applied to the NW device. By controlling the amount of PEO applied to the tip of the micromanipulator, we achieved a small liquid droplet with a size of 20 – 100 μm to minimize leak current. The gate leak current was substantially smaller than the conduction current in all measurements.

Current-voltage curves were measured through a current preamplifier (DL Instruments, model 1211) and a NI data acquisition system. Scanning photocurrent microscopy (SPCM) measurements were performed using a home-built setup based upon an Olympus microscope. Briefly, a 532 nm CW laser was focused by a 100× N.A. 0.95 objective lens to a diffraction limited spot and raster scanned on a planar NW device by a pair of mirrors mounted on galvanometers, while both reflectance and photocurrent were simultaneously recorded to

produce a two-dimensional (2D) maps. The laser intensity was controlled below the threshold of insulator-to-metal transition for all measurements.

# **Supporting Information**

Electron microscopic image of as-grown VO<sub>2</sub> nanowire samples studied, control experimental results demonstrating ion blocking of the PMMA layer, morphology of the VO<sub>2</sub> NW device before and after gating, extraction of simulation parameters, and a table summarizing the diffusion constants measured in all devices. The Supporting Information is available free of charge on the ACS Publications website at http://pubs.acs.org.

## **Notes**

The authors declare no competing financial interest.

## Acknowledgements

This work was supported by the U.S. National Science Foundation Grant DMR-1710737 and the UC Laboratory Fees research program. Work at the Molecular Foundry was supported by the Office of Science, Office of Basic Energy Sciences, of the U.S. Department of Energy under Contract No. DE-AC02-05CH11231.

### References

- (1) Morin, F. J. Phys. Rev. Lett. **1959**, *3*, 34-36.
- (2) Qazilbash, M. M.; Brehm, M.; Chae, B.-G.; Ho, P.-C.; Andreev, G. O.; Kim, B.-J.; Yun, S. J.; Balatsky, A. V.; Maple, M. B.; Keilmann, F.; Kim, H.-T.; Basov, D. N. *Science* **2007**, *318*, 1750-1753.
- (3) Sohn, J. I.; Joo, H. J.; Porter, A. E.; Choi, C.-J.; Kim, K.; Kang, D. J.; Welland, M. E. *Nano Lett.* **2007**, *7*, 1570-1574.
- (4) Tao, Z.; Han, T.-R. T.; Mahanti, S. D.; Duxbury, P. M.; Yuan, F.; Ruan, C.-Y.; Wang, K.; Wu, J. *Phys. Rev. Lett.* **2012**, *109*, 166406.
- (5) Zhu, Z.; Evans, P. G.; Haglund, R. F.; Valentine, J. G. *Nano Lett.* **2017**, *17*, 4881-4885.
- (6) Lv, T. T.; Li, Y. X.; Ma, H. F.; Zhu, Z.; Li, Z. P.; Guan, C. Y.; Shi, J. H.; Zhang, H.; Cui, T. J. Sci. Rep. **2016**, *6*, 23186.
- (7) Zhou, J.; Gao, Y.; Zhang, Z.; Luo, H.; Cao, C.; Chen, Z.; Dai, L.; Liu, X. Sci. Rep. **2013**, *3*, 3029.
- (8) Nakano, M.; Shibuya, K.; Okuyama, D.; Hatano, T.; Ono, S.; Kawasaki, M.; Iwasa, Y.; Tokura, Y. *Nature* **2012**, *487*, 459-462.
- (9) Ma, H.; Hou, J.; Wang, X.; Zhang, J.; Yuan, Z.; Xiao, L.; Wei, Y.; Fan, S.; Jiang, K.; Liu, K. *Nano Lett.* **2017,** *17*, 421-428.
- (10) Guo, H.; Khan, M. I.; Cheng, C.; Fan, W.; Dames, C.; Wu, J.; Minor, A. M. *Nat. Commun.* **2014**, *5*, 4986.
- (11) Manca, N.; Pellegrino, L.; Kanki, T.; Yamasaki, S.; Tanaka, H.; Siri, A. S.; Marré, D. *Adv. Mat.* **2013**, *25*, 6430-6435.
- (12) Manca, N.; Pellegrino, L.; Kanki, T.; Venstra, W. J.; Mattoni, G.; Higuchi, Y.; Tanaka, H.; Caviglia, A. D.; Marré, D. *Adv. Mat.* **2017**, 1701618.
- (13) Dönges, S. A.; Khatib, O.; O'Callahan, B. T.; Atkin, J. M.; Park, J. H.; Cobden, D.; Raschke, M. B. *Nano Lett.* **2016**, *16*, 3029-3035.
- (14) Huber, M. A.; Plankl, M.; Eisele, M.; Marvel, R. E.; Sandner, F.; Korn, T.; Schüller, C.; Haglund, R. F.; Huber, R.; Cocker, T. L. *Nano Lett.* **2016**, *16*, 1421-1427.
- (15) Hilton, D. J.; Prasankumar, R. P.; Fourmaux, S.; Cavalleri, A.; Brassard, D.; El Khakani, M. A.; Kieffer, J. C.; Taylor, A. J.; Averitt, R. D. *Phys. Rev. Lett.* **2007**, *99*, 226401.
- (16) Liu, M.; Hwang, H. Y.; Tao, H.; Strikwerda, A. C.; Fan, K.; Keiser, G. R.; Sternbach, A. J.; West, K. G.; Kittiwatanakul, S.; Lu, J.; Wolf, S. A.; Omenetto, F. G.; Zhang, X.; Nelson, K. A.; Averitt, R. D. *Nature* **2012**, *487*, 345-348.
- (17) Gray, A. X.; Jeong, J.; Aetukuri, N. P.; Granitzka, P.; Chen, Z.; Kukreja, R.; Higley, D.; Chase, T.; Reid, A. H.; Ohldag, H.; Marcus, M. A.; Scholl, A.; Young, A. T.; Doran, A.; Jenkins, C. A.; Shafer, P.; Arenholz, E.; Samant, M. G.; Parkin, S. S. P.; Dürr, H. A. *Phys. Rev. Lett.* **2016**, *116*, 116403.
- (18) Eyert, V. Phys. Rev. Lett. **2011**, 107, 016401.
- (19) Ji, H.; Wei, J.; Natelson, D. *Nano Lett.* **2012**, *12*, 2988-2992.
- (20) Sasaki, T.; Ueda, H.; Kanki, T.; Tanaka, H. Sci. Rep. 2015, 5, 17080.
- (21) Shibuya, K.; Sawa, A. Adv. Electron. Mater. 2016, 2, 1500131.
- (22) Jeong, J.; Aetukuri, N.; Graf, T.; Schladt, T. D.; Samant, M. G.; Parkin, S. S. P. *Science* **2013**, *339*, 1402-1405.
- (23) Chen, S.; Wang, X. j.; Fan, L.; Liao, G.; Chen, Y.; Chu, W.; Song, L.; Jiang, J.; Zou, C. *Adv. Funct. Mater.* **2016**, *26*, 3532-3541.

- (24) Dahlman, C. J.; LeBlanc, G.; Bergerud, A.; Staller, C.; Adair, J.; Milliron, D. J. *Nano Lett.* **2016**, *16*, 6021-6027.
- (25) Passarello, D.; Altendorf, S. G.; Jeong, J.; Rettner, C.; Arellano, N.; Topuria, T.; Samant, M. G.; Parkin, S. S. P. *Nano Lett.* **2017**, *17*, 2796-2801.
- (26) Jeong, J.; Aetukuri, N. B.; Passarello, D.; Conradson, S. D.; Samant, M. G.; Parkin, S. S. P. Proc. Natl. Acad. Sci. 2015, 112, 1013-1018.
- (27) Zhou, Y.; Park, J.; Shi, J.; Chhowalla, M.; Park, H.; Weitz, D. A.; Ramanathan, S. *Nano Lett.* **2015**, *15*, 1627-1634.
- (28) Peng, X.; Yang, Y.; Hou, Y.; Travaglini, H. C.; Hellwig, L.; Hihath, S.; van Benthem, K.; Lee, K.; Liu, W.; Yu, D. *Phys. Rev. Appl.* **2016**, *5*, 054008.
- (29) Lin, J.; Ji, H.; Swift, M. W.; Hardy, W. J.; Peng, Z.; Fan, X.; Nevidomskyy, A. H.; Tour, J. M.; Natelson, D. *Nano Lett.* **2014**, *14*, 5445-5451.
- (30) Hong, W.-K.; Park, J. B.; Yoon, J.; Kim, B.-J.; Sohn, J. I.; Lee, Y. B.; Bae, T.-S.; Chang, S.-J.; Huh, Y. S.; Son, B.; Stach, E. A.; Lee, T.; Welland, M. E. *Nano Lett.* **2013**, *13*, 1822-1828.
- (31) Yoon, H.; Choi, M.; Lim, T.-W.; Kwon, H.; Ihm, K.; Kim, J. K.; Choi, S.-Y.; Son, J. *Nat. Mat.* **2016**, *15*, 1113-1119.
- (32) Wu, C.; Feng, F.; Feng, J.; Dai, J.; Peng, L.; Zhao, J.; Yang, J.; Si, C.; Wu, Z.; Xie, Y. *J. Am. Chem. Soc.* **2011**, *133*, 13798-13801.
- (33) Filinchuk, Y.; Tumanov, N. A.; Ban, V.; Ji, H.; Wei, J.; Swift, M. W.; Nevidomskyy, A. H.; Natelson, D. *J. Am. Chem. Soc.* **2014**, *136*, 8100-8109.
- (34) Liu, S.; Phillabaum, B.; Carlson, E. W.; Dahmen, K. A.; Vidhyadhiraja, N. S.; Qazilbash, M. M.; Basov, D. N. *Phys. Rev. Lett.* **2016**, *116*, 036401.
- (35) Kasirga, T. S.; Coy, J. M.; Park, J. H.; Cobden, D. H. Nanotechnology 2016, 27, 345708.
- (36) Yu, Y.; Yang, F.; Lu, X. F.; Yan, Y. J.; ChoYong, H.; Ma, L.; Niu, X.; Kim, S.; Son, Y.-W.; Feng, D.; Li, S.; Cheong, S.-W.; Chen, X. H.; Zhang, Y. *Nat. Nano.* **2015**, *10*, 270-276.
- (37) Shi, W.; Ye, J.; Zhang, Y.; Suzuki, R.; Yoshida, M.; Miyazaki, J.; Inoue, N.; Saito, Y.; Iwasa, Y. Sci. Rep. **2015**, *5*, 12534.
- (38) Kim, H.; Kim, B. J.; Sun, Q.; Kang, M. S.; Cho, J. H. Adv. Electron. Mater. **2016**, *2*, 1600122.
- (39) Liu, K.; Fu, D.; Cao, J.; Suh, J.; Wang, K. X.; Cheng, C.; Ogletree, D. F.; Guo, H.; Sengupta, S.; Khan, A.; Yeung, C. W.; Salahuddin, S.; Deshmukh, M. M.; Wu, J. *Nano Lett.* **2012**, *12*, 6272-6277.
- (40) Tromp, R. Nat. Mat. 2003, 2, 212-213.
- (41) Rolison, D. R. Science **2003**, 299, 1698-1701.
- (42) Jensen, L. E.; Björk, M. T.; Jeppesen, S.; Persson, A. I.; Ohlsson, B. J.; Samuelson, L. *Nano Lett.* **2004**, *4*, 1961-1964.
- (43) Hofmann, S.; Csányi, G.; Ferrari, A. C.; Payne, M. C.; Robertson, J. *Phys. Rev. Lett.* **2005**, *95*, 036101.
- (44) Barash, D. *IEEE Trans. Pattern Anal. Mach. Intell* **2002**, *24*, 844-847.
- (45) Yao, K.-M.; Habibian, M. T.; O'Melia, C. R. Environ. Sci. Technol. 1971, 5, 1105-1112.
- (46) Islam, M. S.; Fisher, C. A. J. Chem. Soc. Rev. **2014**, 43, 185-204.
- (47) Ala-Nissila, T.; Ferrando, R.; Ying, S. C. Adv. Phys. **2002**, *51*, 949-1078.
- (48) Horch, S.; Lorensen, H. T.; Helveg, S.; Laegsgaard, E.; Stensgaard, I.; Jacobsen, K. W.; Norskov, J. K.; Besenbacher, F. *Nature* **1999**, *398*, 134-136.

- (49) Kellogg, G. L. Surf. Sci. Rep. 1994, 21, 1-88.
- (50) Panitz, J. A. J. Phys. E: Sci. Instrum. 1982, 15, 1281.
- (51) Jardine, A. P.; Hedgeland, H.; Alexandrowicz, G.; Allison, W.; Ellis, J. *Prog. Surf. Sci.* **2009**, *84*, 323-379.
- (52) Ahn, Y.; Dunning, J.; Park, J. *Nano Lett.* **2005**, *5*, 1367-1370.
- (53) Gu, Y.; Romankiewicz, J. P.; David, J. K.; Lensch, J. L.; Lauhon, L. J. *Nano Lett.* **2006,** *6*, 948-952.
- (54) Ahn, Y. H.; Tsen, A. W.; Kim, B.; Park, Y. W.; Park, J. *Nano Lett.* **2007,** *7*, 3320-3323.
- (55) Doh, Y.-J.; Maher, K. N.; Ouyang, L.; Yu, C. L.; Park, H.; Park, J. *Nano Lett.* **2008,** *8*, 4552-4556.
- (56) Allen, J. E.; Hemesath, E. R.; Lauhon, L. J. *Nano Lett.* **2009**, *9*, 1903-1908.
- (57) Graham, R.; Miller, C.; Oh, E.; Yu, D. Nano Lett. 2011, 11, 717-722.
- (58) Putnam, M. C.; Turner-Evans, D. B.; Kelzenberg, M. D.; Boettcher, S. W.; Lewis, N. S.; Atwater, H. A. *Appl. Phys. Lett.* **2009**, *95*, 163116-3.
- (59) Yang, Y.; Peng, X.; Hyatt, S.; Yu, D. *Nano Lett.* **2015**, *15*, 3541-3546.
- (60) Graham, R.; Yu, D. Mod. Phys. Lett. B 2013, 27, 1330018.
- (61) Wang, X.; Gao, H. W. Nano Lett. 2015, 15, 7037-7042.
- (62) Miller, C.; Triplett, M.; Lammatao, J.; Suh, J.; Fu, D.; Wu, J.; Yu, D. *Phys. Rev. B* **2012**, 85, 085111.
- (63) Xu, X.; Yan, M. Y.; Tian, X. C.; Yang, C. C.; Shi, M. Z.; Wei, Q. L.; Xu, L.; Mai, L. Q. *Nano Lett.* **2015**, *15*, 3879-3884.
- (64) Luo, Y.-R., Chapter 11. In *Comprehensive Handbook of Chemical Bond Energies*, CRC Press: 2007; pp 493-569.
- (65) Ip, K.; Overberg, M. E.; Heo, Y. W.; Norton, D. P.; Pearton, S. J.; Stutz, C. E.; Kucheyev, S. O.; Jagadish, C.; Williams, J. S.; Luo, B.; Ren, F.; Look, D. C.; Zavada, J. M. Solid State Electron. 2003, 47, 2255-2259.
- (66) Johnson, O. W.; Paek, S. H.; Deford, J. W. J. Appl. Phys. 1975, 46, 1026-1033.
- (67) Tong, Z.; Hao, J.; Zhang, K.; Zhao, J.; Su, B.-L.; Li, Y. J. Mat. Chem. C 2014, 2, 3651-3658.